How to accurately quantify brain magnetic susceptibility in the context of Parkinson's disease: Validation on phantoms and healthy volunteers at 1.5 and 3 T

Aurélien Hervouin, Johanne Bezy-Wendling, Fanny Noury

Received: 12 February 2024 | Revised: 6 May 2024 | Accepted: 6 May 2024

DOI: 10.1002/nbm.5182

RESEARCH ARTICLE

NMR IN BIOMEDICINE WILEY

How to accurately quantify brain magnetic susceptibility in the context of Parkinson's disease: Validation on phantoms and healthy volunteers at 1.5 and 3 T

Aurélien Hervouin | **Johanne Bézy-Wendling** | **Fanny Noury**

Univ Rennes, Inserm, LTSI-UMR 1099, Rennes, France

Correspondence
Fanny Noury, Univ Rennes, Inserm, LTSI-UMR 1099, 35000 Rennes, France.
Email: fanny.noury@univ-rennes.fr

Funding information
This work received a grant support from the "Défi Scientifique" of the University of Rennes (2022 and 2023).

Abstract

Currently, brain iron content represents a new neuromarker for understanding the physiopathological mechanisms leading to Parkinson's disease (PD). In vivo quantification of biological iron is possible by reconstructing magnetic susceptibility maps obtained using quantitative susceptibility mapping (QSM). Applying QSM is challenging, as up to now, no standardization of acquisition protocols and phase image processing has emerged from referenced studies. Our objectives were to compare the accuracy and the sensitivity of 10 QSM pipelines built from algorithms from the literature, applied on phantoms data and on brain data. Two phantoms, with known magnetic susceptibility ranges, were created from several solutions of gadolinium chelate. Twenty healthy volunteers from two age groups were included. Phantoms and brain data were acquired at 1.5 and 3 T, respectively. Susceptibility-weighted images were obtained using a 3D multigradient-recalled-echo sequence. For brain data, 3D anatomical *T1*- and *T2*-weighted images were also acquired to segment the deep gray nuclei of interest. Concerning in vitro data, the linear dependence of magnetic susceptibility versus gadolinium concentration and deviations from the theoretically expected values were calculated. For brain data, the accuracy and sensitivity of the QSM pipelines were evaluated in comparison with results from the literature and regarding the expected magnetic susceptibility increase with age, respectively. A nonparametric Mann–Whitney *U*-test was used to compare the magnetic susceptibility quantification in deep gray nuclei between the two age groups. Our methodology enabled quantifying magnetic susceptibility in human brain and the results were consistent with those from the literature. Statistically significant differences were obtained between the two age groups in all cerebral regions of interest. Our results show the importance of optimizing QSM pipelines according to the application and the targeted magnetic susceptibility range, to achieve accurate quantification. We

Abbreviations: CN, caudate nucleus; CSF, cerebrospinal fluid; DGN, deep gray nuclei; FSL BET, FMRIB software library brain extraction tool; Gd, gadolinium chelate; GP, globulus pallidus; GRAPPA, generalized autocalibrating partially parallel acquisitions; ICP-MS, inductively coupled plasma mass spectrometry; iLSQR, least-squares; LBV, Laplacian boundary value; MEDI, morphology-enabled dipole inversion; MGRE, multigradient-recalled-echo; PD, Parkinson's disease; PDF, projection-into-dipole-field; Put, putamen; QSM, quantitative susceptibility mapping; RN, red nucleus; ROMEO, rapid opensource minimum spanning tree algorithm; SAG, senior-adults group; SD, standard deviation; SEGUE, speedy region growing algorithm for unwrapping estimated phase; SEPIA, susceptibility mapping pipeline tool for phase images; SHARP, sophisticated harmonic artifact reduction on phase data; SMV, spherical mean value; SN, substantia nigra; STN, subthalamic nucleus; SWI, susceptibility-weighted image; TKD, truncated k-space division; YAG, young-adults group.

were able to define the optimal QSM pipeline for future applications on patients with PD.

KEYWORDS
aging, healthy volunteers; human brain; magnetic susceptibility; Parkinson's disease; phantoms; quantitative MRI; *T2**

1 | INTRODUCTION

It is widely accepted that the neurodegenerative process of Parkinson's disease (PD) begins at least 20 years before the first motor signs appear.[1,2] During this prodromal phase, several pathophysiological mechanisms have been identified, such as abnormally high levels of iron observed in the deep gray nuclei (DGN),[3,4] particularly in the substantia nigra (SN), resulting in damage to dopaminergic neurons.[5] Iron plays a major role in many physiological brain functions, such as the synthesis of neurotransmitters, but its abnormal accumulation in biological tissues causes a cascade of oxidative reactions and neurotoxicity leading to neuronal apoptosis. This progression of the neurodegenerative process in PD is still difficult to predict, and clinicians need reliable neuromarkers to predict the evolution of PD. Currently, the in vivo quantification of iron concentration in the targeted brain regions represents a promising neuromarker for understanding the mechanisms at the origin of the disease and to help its early diagnosis, that is, before the appearance of the first motor symptoms.[6,7]

In vivo quantification of biological iron content is possible using magnetic resonance imaging (MRI), by reconstructing magnetic susceptibility maps obtained using quantitative susceptibility mapping (QSM) methods. In MRI, the magnetic field disturbances associated with susceptibilities are well known and often need to be corrected. But they can also be used to highlight specific structures or tissues, and to detect anatomical or physiological changes on susceptibility-weighted images (SWIs). Given the originality of the information it can provide, this innovative quantitative method is of great interest compared with conventional MRI methods (*T1*, *T2*, diffusion) and currently represents a major turning point in clinical research, particularly in neurological applications. Over the last 10 years, QSM has been applied to a wide variety of pathologies, such as hepatic fibrosis[8] and neurodegenerative diseases like Alzheimer's disease[9] and microbleeds.[10] QSM has been also used for early detection of PD,[11] as it was demonstrated to be more sensitive and accurate than *R2**.[12–14] Several studies have shown a significant increase in magnetic susceptibility values in the SN in the early stages of PD compared with control groups, as well as the possibility of differentiating between the stages of progression of PD.[5,15] Other DGN, such as the globulus pallidus (GP), caudate nucleus (CN), and putamen (Put), have also been targeted.[3,4] This quantitative MRI method can also be used to evaluate neurological aging, as normal brain iron deposition increases over the years.[16,17]

Most clinical applications depend on the magnitude images, but in QSM the information is contained in the phase images, which require specific processing algorithms.[4,18] Reconstructing QSM maps is a challenge, as some publications revealed a true lack of standardization regarding the acquisition protocols and phase image processing,[16,19] even although these two points are essential for achieving accurate magnetic susceptibility quantification.[20] As there is no standardization of QSM pipelines, it is difficult to have a gold standard of in vivo magnetic susceptibility values of human brain. Recently, to move towards standardization of image acquisition and reconstruction methods, recommended implementation of QSM for clinical brain research has been proposed following a consensus of the International Society of Magnetic Resonance in Medicine–Electro-Magnetic Tissue Properties Study Group.[19]

The optimal way to standardize quantitative MRI methods is to validate them first on specific phantoms suitable for the clinical topic of interest, and then on healthy volunteers before considering applications on patients. Both the acquisition protocol and the processing pipeline of MRI data must be optimized, but the processing pipeline remains the first step to optimize, as it is needed to analyze and compare data acquired using various acquisition parameters.

In this general context, the aim of our study was to compare the accuracy of QSM pipelines in the particular application of aging and PD. We chose to work with a standard acquisition protocol based on a multigradient-recalled-echo (MGRE) with eight echoes, as this sequence is particularly sensitive to MR signal modifications resulting from magnetic susceptibility variations in biological tissues, and is widely used at 3 T in clinical research. An in-depth analysis of the literature enabled the selection of 15 algorithms, which were combined in 10 QSM pipelines in the same processing software.[18] Our strategy was first to work with two phantoms with known magnetic susceptibility ranges corresponding to the susceptibility values of the targeted DGN in PD, and then to acquire in vivo data on healthy volunteers from two age groups. The objective of the first step was to verify the robustness of the chosen algorithms and the influence of the magnetic susceptibility range on the efficiency of the various pipelines. The second step enabled us to study the effect of in vivo constraints such as the structure and composition of biological tissues, as well as the size and shape of the brain regions of interest, on the performances of the QSM pipelines. Concerning in vivo data, we chose to investigate the accuracy and sensitivity of the 10 QSM pipelines by comparing our results with several studies from the literature (magnetic susceptibility ranges and consistency of the susceptibility graduation in the DGN) and by studying their ability to distinguish two age groups.

The final objective of this work will be to apply our methodology for in vivo quantification of magnetic susceptibility in DGN to cohorts of patients to explore the potential of this new neuromarker for monitoring PD progression and identifying diverse profiles in patients with PD.[21]

2 | MATERIALS AND METHODS

2.1 | Phantoms

The magnetic susceptibility of a solution of gadolinium chelate (Gd) linearly depends on its concentration.[22] Two phantoms with known magnetic susceptibility ranges were then created, each containing seven tubes (diameter: 10 mm, length: 70 mm): one was filled with distilled water and the other six with distilled water solutions of Dotarem (Gadoterate Meglumine; 0.5 $mmoL \cdot mL^{-1}$; Guerbet, France). These seven tubes were then placed in a container of 50-mm diameter filled with distilled water to avoid magnetic susceptibility artifacts around them, due to the abrupt transition of susceptibility between air and liquid. The first phantom included solutions with an in vivo magnetic susceptibility range corresponding to the DGN (phantom 1) and the second phantom included solutions with a higher magnetic susceptibility range (phantom 2). Gd concentrations (Table 1) and geometries of the phantoms were chosen from the literature.[22]

The Gd concentration of each solution was analyzed using inductively coupled-plasma mass spectrometry (ICP-MS; Agilent 7900, LERES) as a reference method. The sample of Gd solution was nebulized, and the formed aerosol transported into a plasma torch, where processes such as evaporation, dissociation, atomization, and ionization take place. The ions focused in the spectrometer are separated based on their mass-to-charge ratio. The limit of quantification for gadolinium is 0.1 $\mu g \cdot L^{-1}$. The LERES laboratory (EHESP; Irset UMR_S 1085 Inserm, Rennes, France) is accredited to NF EN ISO 17025 by the French Accreditation Committee (COFRAC).

2.2 | Healthy volunteers

Twenty healthy volunteers with no history of neurological disorder were recruited from May 2021 to June 2023 (clinical trial NCT-05107232; Rennes University Hospital) and written informed consent was obtained from all participants. Two groups were constituted: the senior-adults group (SAG; $n = 10$; male:female = 1:1; age = 46.3 ± 3.8 years) and the young-adults group (YAG; $n = 10$; male:female = 1:1; age = 23.6 ± 1.2 years).

2.3 | MRI data acquisition

For this preliminary study before in vivo application on patients with PD, we chose to acquire in vitro data using a 1.5-T MRI device dedicated to animal imaging, and in vivo data using a 3-T MRI device of the University Hospital. As the magnetic susceptibility does not depend on the magnetic field strength,[23] the results of this two-part study could be compared.

2.3.1 | Phantoms

SWIs were acquired in magnitude and phase modes on a 1.5-T MRI device dedicated to animal imaging (Magnetom Avanto; Siemens, Erlangen, Germany) equipped with a 40 $mT \cdot m^{-1}$ gradient system and a Siemens Symphony High Resolution Wrist Array. A 3D MGRE sequence in axial orientation was used with a spatial resolution of $(1.64\ mm)^3$, a bandwidth of 200 Hz/pixel, and a generalized autocalibrating partially parallel acquisitions (GRAPPA) acceleration factor of 2. The acquisition parameters are detailed in Table 2. This protocol was repeated during five different MRI sessions for each phantom.

TABLE 1 Concentration ranges of Gd (mM) and corresponding ranges of MS (ppm) for the two phantoms: one phantom with a MS range close to the cerebral regions of interest (phantom 1) and one phantom with a higher MS range (phantom 2).

	Phantom 1						Phantom 2					
[Gd] (mM)	0.010	0.050	0.100	0.200	0.400	0.600	1.000	2.000	4.000	6.000	8.000	10.000
Magnetic susceptibility (ppm)	0.003	0.016	0.033	0.065	0.130	0.196	0.326	0.652	1.304	1.956	2.608	3.260

Abbreviations: Gd, gadolinium chelate; MS, magnetic susceptibility.

2.3.2 | Healthy volunteers

Brain MR images were acquired on a 3-T MRI device (Magnetom Prisma VE11C; Siemens Healthineers, Erlangen, Germany) equipped with a 64-channel head coil. The acquisition protocol included 3D anatomical *T1*- and *T2*-weighted (T1w and T2w) images with a spatial resolution of $(1\ mm)^3$ to segment the DGN of interest. Several SWIs were acquired in magnitude and phase modes, using a 3D MGRE sequence in axial orientation with a spatial resolution of $(1.5\ mm)^3$, a bandwidth of 200 Hz/pixel, a GRAPPA acceleration factor of 2, and without fat saturation or flow compensation. The acquisition parameters of T1w and T2w images and SWIs are listed in Table 2.

2.4 | MRI data analysis

2.4.1 | DGN segmentation for healthy volunteers

The segmentation of the DGN was carried out from anatomical images. Three regions per hemisphere (CN, Put, GP) were segmented from the T1w images using the *recon-all* process of FreeSurfer (version 7.2.0).[24] Three additional regions per hemisphere (SN, red nucleus [RN], and subthalamic nucleus [STN]) were segmented from the T2w images using pBrain (version 1.0).[25] These two segmentations were merged in a unique segmentation file using 3D Slicer (version 4.11; https://www.slicer.org/) and then overlaid on QSM maps (Figure 1).

2.4.2 | QSM maps reconstruction

All computations were performed on Matlab (version 2017Rb; MathWorks, Natick, MA, USA) using the SEPIA software package[18] to reconstruct QSM maps from the phase and magnitude images of SWI data. Ten QSM pipelines, including different combinations of various algorithms from the literature, were compared for the four consecutive steps of QSM maps reconstruction: masking, phase unwrapping, background field removal, and field to susceptibility inversion (Table 3). Every parameter was optimized in a previous in-house study to determine the appropriate regularization parameters. For the morphology-enabled dipole inversion (MEDI) phase unwrapping method, the regularization parameter lambda was tested at 100, 200, 300, 400, 500, 1000, 2000, 5000, 10,000, and 50,000. The spherical mean value (SMV) radius was tested between 1 and 6 mm, every millimeter and 10 mm.

Several of these nonexhaustive pipelines were used in the literature to quantify magnetic susceptibility in the human brain.[4,12,16,37]

First, the FMRIB software library brain extraction tool (FSL BET)[38] was manually settled to be adapted to the phantom shape (threshold of 0.01). For the data of healthy volunteers, automatic FSL BET parameters were used. Then the phase image was unwrapped using either a 3D-Laplacian-based method[27,28] or a spatial domain unwrapping recent algorithms such as a speedy region growing algorithm for unwrapping estimated phase (SEGUE)[29] and a path-based unwrapping rapid opensource minimum spanning tree algorithm (ROMEO).[30] The standard parameters were applied for each of these algorithms.

For the third step of background field removal, we tested the projection-into-dipole-field (PDF),[32] the Laplacian boundary value (LBV),[33] the sophisticated harmonic artifact reduction on phase data (SHARP)[34] and its additional variations, variable-kernel SHARP (V_SHARP)[31] and regularization-enabled SHARP (RESHARP).[34] For PDF we used a tolerance of 0.1, 30 iterations, and a zeropad size of 40. The LBV parameters were a tolerance of 0.0001, a depth of 5, and a peel of 2. For SHARP, we used an SMV radius of 6 mm and a threshold of 0.03. The SMV radius of V-SHARP was fixed to be 25 mm. For RESHARP, the SMV radius was fixed to be 4 mm with a regularization parameter of 0.05.

Finally, the field-to-susceptibility inversion was processed with the MEDI,[27] the truncated k-space division (TKD),[36] the least-squares (iLSQR)[31] or the streaking artifact reduction for QSM (Star-QSM)[35] method. For MEDI, we chose a lambda parameter of 1000 and a SMV radius of 5 mm. For TKD, the dipole truncation parameter was set to 0.33. For Star-QSM, the pad-size parameter was set to 12. For iLSQR, a threshold of 0.01 was used, with a maximum iteration of 100.

2.4.3 | Magnetic susceptibility quantification

For the two phantoms, the mean magnetic susceptibility values and standard deviation (SD) of the seven tubes were quantified from QSM maps using the ImageJ (version 1.53g; National Institute of Health) software. A region of interest was manually drawn on each of the seven tubes. The absolute quantitative data were analyzed with Microsoft Excel (version 2019; Microsoft Office). To evaluate the accuracy of the 10 QSM pipelines, a deviation from the theoretically expected values was calculated for the tube filled with distilled water and the six Gd solutions, then the linear regression of magnetic susceptibility values versus Gd concentration was plotted.

TABLE 2 Details of the acquisition parameters used for the MRI protocols applied on the two phantoms (1.5 T) and the 20 healthy volunteers of the young-adults group and the senior-adults group (3 T).

	Magnetic field (T)	MRI sequence	Number of echoes	$TE_{min}/\Delta TE$ (ms)	TR (ms)	Flip angle (°)	FOV (mm^3)	Matrix	Spatial resolution (mm^3)	Inversion time (ms)	Acquisition time (min:s)
Phantoms	1.5	SWI MGRE	8/monopolar	7/6	72	20	210 × 210 × 105	128 × 128 × 64	1.64 × 1.64 × 1.64	-	4:12
Healthy volunteers	3.0	SWI MGRE	8/monopolar	3.6/5.9	55	15	192 × 192 × 156	128 × 128 × 104	1.50 × 1.50 × 1.50	-	6:31
		T_1w MPRAGE	-	2.3	1900	9	256 × 256 × 176	256 × 256 × 176	1.00 × 1.00 × 1.00	900	4:26
		T_2w TSE	-	407	2700	90	256 × 256 × 176	256 × 256 × 176	1.00 × 1.00 × 1.00	-	4:42

Abbreviations: FOV, field of view; MGRE, multigradient-recalled-echo; MPRAGE, Magnetization Prepared RApid Gradient Echo; MRI, magnetic resonance imaging; SWI, susceptibility-weighted images; T_1w, T1-weighted; T_2w, T2-weighted; TSE, turbo spin echo.

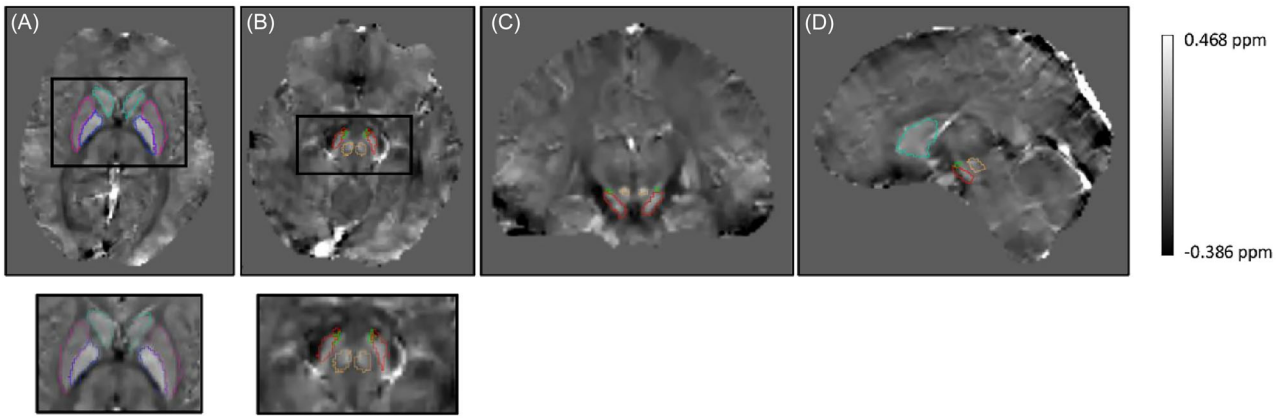

FIGURE 1 Example of the segmentation process for one subject from the senior-adults group: the deep gray nuclei were segmented from T1w and T2w images, then overlaid on the quantitative susceptibility mapping (QSM) map. (A) Globulus pallidus (GP) (blue), putamen (rose), and caudate nucleus (CN) (turquoise), segmented from the T1w image, are observed on the QSM map in axial orientation (slice 49/104; 4.78 mm). (B) Substantia nigra (SN) (red), red nucleus (RN) (orange), and subthalamic nucleus (STN) (green), segmented from the T2w image, are observed in the QSM map in axial orientation (slice 41/104; −7.22 mm). (C) SN, RN, and STN observed on the QSM map in coronal orientation (slice 60/128; −2.73 mm). (D) CN, SN, RN, and STN observed on the QSM map in sagittal orientation (slice 67/128; −2.13 mm). T_1w, T1-weighted; T_2w, T2-weighted.

TABLE 3 Details of the 10 QSM pipelines tested on the susceptibility-weighted images data acquired on the two phantoms and the 20 healthy volunteers of the young-adults group and the senior-adults group. These pipelines include different algorithms from the literature for the three steps of the QSM maps calculation: phase unwrapping, background field removal, and field-to-susceptibility inversion.

Pipelines	1	2	3	4	5[16]	6[4]	7[4]	8[4]	9[26]	10[12]
Step 1: phase unwrapping	Laplacian MEDI[27,28]	Region growing	SEGUE[29]	ROMEO[30]	Laplacian—MEDI[27,28]				Laplacian STI[31]	SEGUE[29]
Step 2: background field removal	PDF[32]		LBV[33]	PDF[32]	V-SHARP[31]	LBV[32]		SHARP[34]	V-SHARP[31]	RESHARP[34]
Step 3: field-to-susceptibility inversion	MEDI[27,28]				Star-QSM[35]	MEDI[27,28]	TKD[36]	MEDI[27,28]	iLSQR[31]	TKD[36]

Abbreviations: iLSQR, least-squares; LBV, Laplacian boundary value; MEDI, morphology-enabled dipole inversion; PDF, projection-into-dipole-field; QSM, quantitative susceptibility mapping; RESHARP, regularization-enabled SHARP; ROMEO, rapid opensource minimum spanning tree algorithm; SEGUE, speedy region growing algorithm for unwrapping estimated phase; SHARP, sophisticated harmonic artifact reduction on phase data; Star-QSM, streaking artifact reduction for QSM; STI, susceptibility tensor imaging from STI suite; TKD, truncated k-space division; V-SHARP, variable-kernel SHARP.

For each healthy volunteer, the mean magnetic susceptibility values and SD of each DGN were quantified from the QSM maps and the segmentation file using 3D Slicer (version 4.11). These results were averaged for each of the DGN between left and right hemispheres and referenced to the whole-brain magnetic susceptibility value.[16] The quantitative data were analyzed with Microsoft Excel (version 2019; Microsoft Office). A statistical analysis using a nonparametric Mann-Whitney *U*-test (maximum risk α of 0.05) was carried out to compare the magnetic susceptibility values in each of the DGN between the YAG and the SAG.

2.4.4 | T_2^* quantification

For each healthy volunteer, the mean *T2** and SD values of each of the DGN were quantified from the SWI in magnitude and the segmentation file by a monoexponential regression of signal versus *TE* using 3D Slicer (version 4.11). These results were averaged for each DGN between left and right hemispheres. For the nonparametric Mann–Whitney *U*-test, *T2** values quantified in each of the DGN were divided by the whole-brain *T2** values.

3 | RESULTS

3.1 | Phantoms

Figure 2 shows the QSM maps calculated for phantom 1 (Figure 2A) and phantom 2 (Figure 2B) using pipelines 1 to 5, 7, and 9. Concerning pipelines 6 and 8, the software completed successfully, but generated a "black screen" QSM map. For phantom 2, pipeline 10 generated an exploitable QSM map, but not for phantom 1, so we decided to eliminate this pipeline because of the specific application of our study on PD and magnetic susceptibility quantification in DGN.

Figure 3 displays the linear regression of magnetic susceptibility values versus concentration of Gd for pipelines 1 to 5, 7, and 9, as well as the parameters of the regression and the deviation from the theoretically expected values for each Gd solution. As expected, a linear dependence is observed for each pipeline and each phantom. For phantom 1 (Figure 3A), pipeline 1 showed globally the smallest values of deviations from the theoretically expected values. This pipeline had an optimal linear regression ($R^2 = 0.984$) with a slope of 0.226 ppm·mM^{-1}, close to the theoretical value of 0.326 ppm·mM^{-1}[22] and a minimal intercept value of 0.010 ppm. Pipeline 2 had the same slope (0.226 ppm·mM^{-1}), but presented an intercept value of −0.054 ppm with the theoretical value, meaning that this pipeline was not optimal for this magnetic susceptibility range. For phantom 2 (Figure 3B), pipeline 2 showed an optimal linear regression ($R^2 = 0.856$) with a slope of 0.291 ppm·mM^{-1}, close to the theoretical

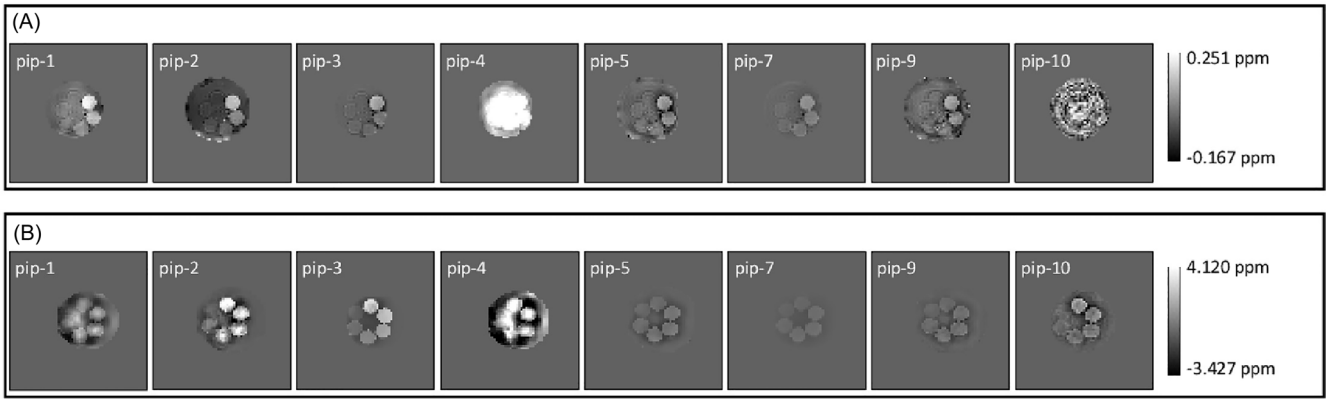

FIGURE 2 Quantitative susceptibility mapping (QSM) maps reconstructed using the pipelines 1 to 5, 7, and 9 for the two phantoms: (A) Phantom 1, and (B) Phantom 2. Pipelines 6 and 8 did not generate QSM maps. pip, pipeline.

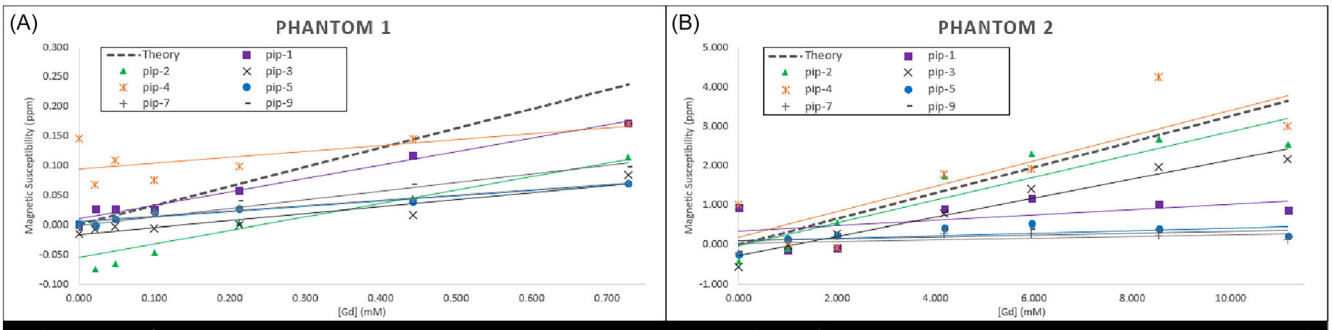

PHANTOM 1	Theory	pip-1	pip-2	pip-3	pip-4	pip-5	pip-7	pip-9
a	0.326	0.226	0.226	0.119	0.099	0.089	0.089	0.144
b	0.000	0.010	-0.054	-0.016	0.094	0.004	0.005	-0.001
R^2	1.000	0.984	0.834	0.885	0.477	0.949	0.920	0.958
[Gd] (mM)	MS (ppm)	*Deviation from the theoretically expected values (ppm)*						
0.022	**0.007**	0.019	-0.082	-0.015	0.061	-0.008	-0.006	-0.015
0.048	**0.016**	0.012	-0.081	-0.019	0.093	-0.006	0.004	-0.008
0.100	**0.033**	-0.007	-0.080	-0.039	0.043	-0.011	-0.012	-0.011
0.213	**0.069**	-0.011	-0.066	-0.070	0.029	-0.042	-0.041	-0.030
0.443	**0.144**	-0.028	-0.100	-0.129	0.001	-0.106	-0.101	-0.077
0.728	**0.237**	-0.065	-0.124	-0.153	-0.067	-0.167	-0.168	-0.140

PHANTOM 2	Theory	pip-1	pip-2	pip-3	pip-4	pip-5	pip-7	pip-9
a	0.326	0.067	0.291	0.244	0.323	0.033	0.021	0.024
b	0.000	0.349	-0.039	-0.286	0.182	0.092	0.040	0.100
R^2	1.000	0.263	0.856	0.962	0.719	0.277	0.237	0.235
[Gd] (mM)	MS (ppm)	*Deviation from the theoretically expected values (ppm)*						
1.000	**0.326**	-0.449	-0.422	-0.328	-0.310	-0.173	-0.248	-0.182
2.000	**0.652**	-0.747	-0.090	-0.382	-0.730	-0.408	-0.449	-0.398
4.185	**1.364**	-0.458	0.363	-0.578	0.415	-0.938	-1.098	-0.981
5.956	**1.942**	-0.774	0.363	-0.544	-0.030	-1.410	-1.665	-1.549
8.540	**2.784**	-1.776	-0.113	-0.831	1.456	-2.387	-2.555	-2.473
11.161	**3.638**	-2.782	-1.103	-1.484	-0.632	-3.424	-3.517	-3.450

FIGURE 3 Linear regression of magnetic susceptibility values versus concentration of gadolinium chelate (Gd) for pipelines 1 to 5, 7, and 9, as well as the parameters of the regression and the deviations from the theoretically expected values for each Gd solution, for (A) Phantom 1, and (B) Phantom 2. pip, pipeline.

value and a minimal intercept value of −0.039 ppm. Pipeline 1 gave coherent magnetic susceptibility values for concentrations lower than 4.185 mM, showing the dependence of phase unwrapping methods accuracy on the targeted magnetic susceptibility range. Despite an interesting slope of 0.323 ppm·mM^{-1}, pipeline 4 had a weak correlation coefficient ($R^2 = 0.719$) and so was not optimal for this magnetic susceptibility range.

3.2 | Healthy volunteers

3.2.1 | Magnetic susceptibility quantification

Figures 4A and 5A show examples of the QSM maps calculated using pipelines 1 to 10 for one subject of the YAG and the SAG, respectively. We decided to exclude pipeline 7 because of the qualitative blurry aspect of the corresponding QSM maps observed for each healthy volunteer, leading to an inaccurate quantification.

Table 4 provides an overview of the magnetic susceptibility quantification, presenting mean susceptibility and SD for each DGN of the YAG and the SAG. These results were compared with magnetic susceptibility values from the literature using studies conducted by Guan et al.[16] (pipeline 5), Santin et al.[4] (pipeline 6), and Mao et al.[26] (pipeline 9). Generally, pipelines 1 and 2 exhibited lower magnetic susceptibility values than the referenced studies, in both the YAG and the SAG, for the majority of DGN. To illustrate this, the magnetic susceptibility values quantified in the SN by pipeline 1 were 0.019 ± 0.042 ppm (vs. 0.076 ppm[16] and 0.074 ± 0.024 ppm[4]) for the YAG, and 0.052 ± 0.065 ppm (vs. 0.090 ppm[16] and 0.097 ± 0.023 ppm[26]) for the SAG. Pipelines 4, 6, and 8 demonstrated better performances in the quantification of magnetic susceptibility among the 10 pipelines, giving results close to those from the literature. Despite the variability in existing references, these three pipelines consistently delivered results within the reported ranges from the literature for all targeted DGN. For example, concerning RN, pipeline 4 exhibited magnetic

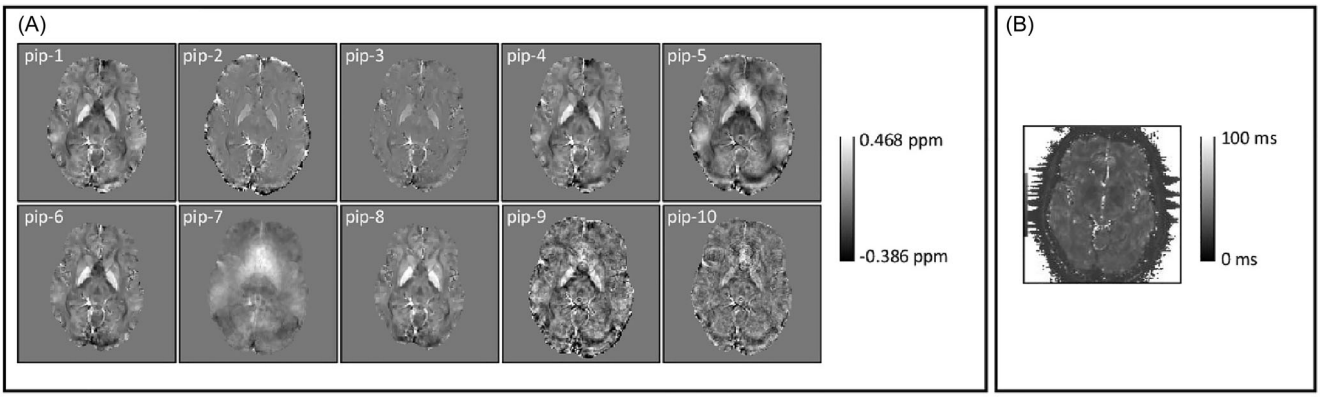

FIGURE 4 Example of the in vivo (A) Quantitative susceptibility mapping (QSM) maps, and (B) the *T2** map calculated for one healthy volunteer from the young-adults group. The QSM maps were reconstructed using pipelines 1 to 10. pip, pipeline.

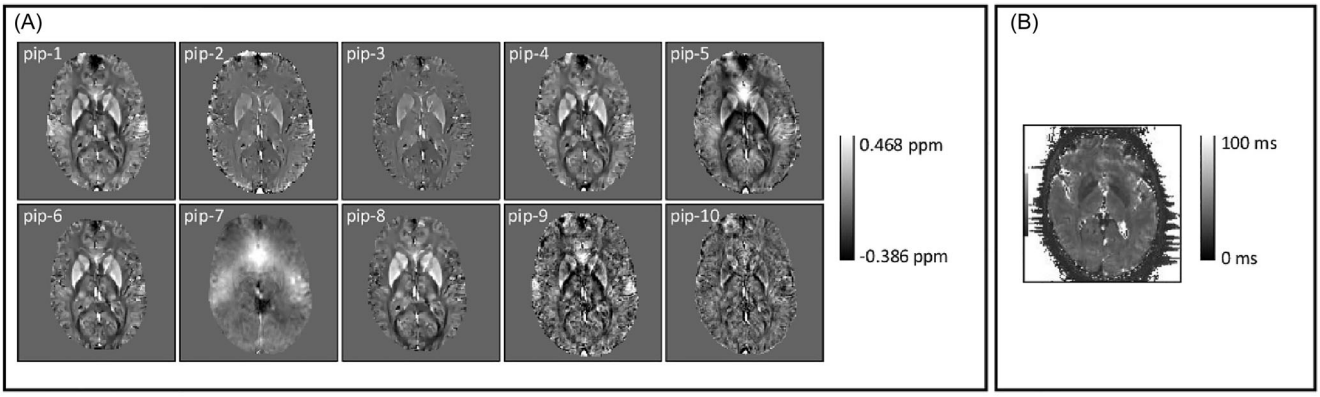

FIGURE 5 Example of the in vivo (A) Quantitative susceptibility mapping (QSM) maps, and (B) The *T2** map calculated for one healthy volunteer from the senior-adults group. The QSM maps were reconstructed using pipelines 1 to 10. pip, pipeline.

TABLE 4 Mean magnetic susceptibility values and SD (ppm) quantified using the pipelines 1 to 6 and 8 to 10, in each targeted DGN, compared with references from the literature.[4,16,26] Mean T_2* values and SD (ms) quantification, compared with references from the literature.[4,39]

		Mean magnetic susceptibility and SD (ppm)											Mean T_2* and SD (ms)	
Pipelines		1	2	3	4	5	6	8	9	10	Guan et al.[16]	YAG: Santin et al.[4] SAG: Mao et al.[26]	This study	YAG: Santin et al.[4] SAG: Guan et al.[39]
Put	YAG	−0.002 ± 0.032	0.003 ± 0.005	0.004 ± 0.003	0.022 ± 0.008	0.002 ± 0.005	0.023 ± 0.007	0.030 ± 0.008	0.008 ± 0.004	−0.002 ± 0.003	0.012	0.056 ± 0.011	47.53 ± 4.35	43.48 ± 1.00
	SAG	0.028 ± 0.024	0.018 ± 0.010	0.022 ± 0.010	0.052 ± 0.016	0.022 ± 0.010	0.055 ± 0.015	0.060 ± 0.015	0.028 ± 0.009	0.010 ± 0.013	0.030	0.045 ± 0.014	37.67 ± 4.28	33.60 ± 3.50
CN	YAG	0.037 ± 0.021	0.011 ± 0.004	0.011 ± 0.004	0.036 ± 0.009	0.016 ± 0.014	0.035 ± 0.008	0.039 ± 0.009	0.044 ± 0.009	0.023 ± 0.004	0.022	0.057 ± 0.013	52.65 ± 4.17	45.45 ± 1.00
	SAG	0.051 ± 0.021	0.020 ± 0.008	0.022 ± 0.007	0.049 ± 0.011	0.024 ± 0.009	0.050 ± 0.010	0.054 ± 0.011	0.046 ± 0.009	0.029 ± 0.006	0.029	0.033 ± 0.010	43.97 ± 4.18	39.21 ± 1.25
RN	YAG	0.030 ± 0.047	0.027 ± 0.013	0.026 ± 0.013	0.048 ± 0.019	0.028 ± 0.014	0.051 ± 0.020	0.062 ± 0.021	0.058 ± 0.021	0.032 ± 0.014	0.044	0.035 ± 0.018	37.05 ± 4.38	40.00 ± 0.33
	SAG	0.062 ± 0.040	0.038 ± 0.022	0.047 ± 0.019	0.077 ± 0.032	0.052 ± 0.028	0.077 ± 0.027	0.088 ± 0.029	0.077 ± 0.022	0.049 ± 0.028	0.070	0.085 ± 0.026	34.86 ± 13.10	28.17 ± 4.51
STN	YAG	−0.004 ± 0.046	0.014 ± 0.013	0.015 ± 0.012	0.034 ± 0.030	0.009 ± 0.021	0.036 ± 0.027	0.049 ± 0.031	0.023 ± 0.034	0.027 ± 0.023	-	0.040 ± 0.020	34.85 ± 3.58	37.74 ± 0.50
	SAG	0.040 ± 0.050	0.032 ± 0.021	0.036 ± 0.016	0.072 ± 0.023	0.035 ± 0.016	0.068 ± 0.026	0.075 ± 0.024	0.055 ± 0.021	0.048 ± 0.017	-	-	30.33 ± 3.23	-
SN	YAG	0.019 ± 0.042	0.024 ± 0.006	0.025 ± 0.007	0.049 ± 0.016	0.028 ± 0.007	0.054 ± 0.016	0.066 ± 0.020	0.049 ± 0.020	0.040 ± 0.008	0.076	0.074 ± 0.024	32.87 ± 2.51	37.74 ± 0.50
	SAG	0.052 ± 0.065	0.031 ± 0.022	0.036 ± 0.025	0.077 ± 0.035	0.043 ± 0.034	0.076 ± 0.034	0.085 ± 0.033	0.076 ± 0.028	0.059 ± 0.027	0.090	0.097 ± 0.023	33.57 ± 7.74	38.46 ± 2.50
GP	YAG	0.046 ± 0.041	0.026 ± 0.008	0.027 ± 0.008	0.079 ± 0.014	0.030 ± 0.009	0.082 ± 0.013	0.091 ± 0.015	0.056 ± 0.011	0.024 ± 0.005	0.075	0.090 ± 0.023	33.17 ± 2.71	33.33 ± 0.33
	SAG	0.070 ± 0.039	0.036 ± 0.015	0.040 ± 0.014	0.102 ± 0.021	0.042 ± 0.015	0.106 ± 0.021	0.112 ± 0.020	0.064 ± 0.011	0.034 ± 0.023	0.105	0.091 ± 0.020	29.60 ± 3.30	23.52 ± 7.14

Abbreviations: CN, caudate nucleus; DGN, deep gray nuclei; GP, globulus pallidus; Put, putamen; RN, red nucleus; SAG, senior-adults group; SD, standard deviation; SN, substantia nigra; STN, subthalamic nucleus; YAG, young-adults group.

susceptibility values of 0.077 ± 0.032 ppm (vs. 0.070 ppm[16] and 0.085 ± 0.026 ppm[26]) for the SAG. Pipeline 6 obtained magnetic susceptibility values in GP of 0.082 ± 0.013 ppm for the YAG (in comparison with 0.075 ppm[16] and 0.090 ± 0.023 ppm[4]). For SN, pipeline 8 obtained magnetic susceptibility values of 0.085 ± 0.033 ppm (vs. 0.090 ppm[16] and 0.097 ± 0.023 ppm[26]) for the SAG. Furthermore, an age-related increase of magnetic susceptibility was observed for most pipelines in each DGN, indicating a global trend of rising magnetic susceptibility with age.

Table 5 presents the outcomes of the statistical analysis between the YAG and the SAG of magnetic susceptibility values quantified using the 10 pipelines. Statistically significant differences ($p < 0.05$) were obtained for most of them in the DGN of interest. Pipeline 8 showed a statistically significant increase of magnetic susceptibility values with age in Put ($p < 0.01$), CN ($p < 0.02$), GP ($p < 0.02$), and RN ($p < 0.05$). Pipeline 6 obtained a statistically significant increase between the YAG and the SAG for five of the six DGN, with a p value of less than 0.05 in the STN. The best results were observed using pipeline 4, with a statistically significant increase of magnetic susceptibility values with age in all the DNG of interest: we observed the same statistical threshold than in pipeline 6 in Put ($p < 0.01$) and RN ($p < 0.05$), a p value of less than 0.01 in STN, and of less than 0.02 in CN and GP. Pipeline 4 was the only one to show a statistically significant difference in magnetic susceptibility values with age in SN ($p < 0.05$), which is particularly relevant in the context of applications on PD.

3.2.2 | T_2^* quantification

Figures 4B and 5B display an example of the $T2^*$ map calculated for one subject of the YAG and one subject of the SAG, respectively. Table 4 presents mean $T2^*$ values and SD in the targeted DGN, which were consistent with those from the literature.[4,39] As the $T2^*$ map was also calculated from SWIs, these results provide a quality control of our data acquired using a standard MGRE protocol with height monopolar echoes. Overall, a general decrease in $T2^*$ values with age was observed as expected, because of the presumed higher iron concentration in the DGN of interest for the SAG, resulting in a greater field disruption.

Table 5 presents the outcomes of the statistical analysis of $T2^*$ values in each of the DGN between the YAG and the SAG. Statistically significant differences were obtained for all the DGN, except for the SN: Put, CN and STN ($p < 0.01$), GP ($p < 0.02$), and RN ($p < 0.05$).

4 | DISCUSSION

Concerning the performances of the various algorithms tested in our study, for phantoms, and particularly for phantom 1, pipeline 1 was the most accurate among all pipelines (especially for a magnetic susceptibility range similar to the one expected in DGN), and pipeline 2 was also very precise (especially on a superior range of magnetic susceptibility). These pipelines both use the PDF[32] algorithm as the background field-removal step. Here, the performance of PDF was good, in line with similar observations in phantoms in the literature.[40–42] Despite these in vitro observations, pipelines 1 and 2 gave inaccurate results for data acquired on healthy volunteers (Table 4), showing lower magnetic susceptibility values compared with ranges from the literature. This can be explained not only by the shape of the DGN, where boundaries between areas with

TABLE 5 Results of the statistical analysis performed using a nonparametric Mann–Whitney U-test (risk $\alpha = 0.05$). Concerning magnetic susceptibility quantification, statistically significant differences between the two age groups were obtained for several or all DGN for pipelines 2 to 6 and 8 to 10. For T_2^* quantification, statistically significant differences between the young-adults group and the senior-adults group were observed for five of the six DGN of interest.

	Pipelines	Put	CN	RN	STN	SN	GP
Magnetic susceptibility	1	-	-	-	-	-	-
	2	$p < 0.01$	$p < 0.02$	-	$p < 0.05$	-	-
	3	$p < 0.01$	$p < 0.01$	$p < 0.05$	$p < 0.01$	-	$p < 0.02$
	4	$p < 0.01$	$p < 0.02$	$p < 0.05$	$p < 0.01$	$p < 0.05$	$p < 0.02$
	5	$p < 0.01$	$p < 0.05$	$p < 0.05$	$p < 0.01$	-	-
	6	$p < 0.01$	$p < 0.01$	$p < 0.05$	$p < 0.05$	-	$p < 0.01$
	8	$p < 0.01$	$p < 0.02$	$p < 0.05$	-	-	$p < 0.02$
	9	$p < 0.01$	-	$p < 0.05$	$p < 0.01$	$p < 0.02$	-
	10	$p < 0.01$	$p < 0.02$	-	$p < 0.05$	$p < 0.05$	-
T_2^*	-	$p < 0.01$	$p < 0.01$	$p < 0.05$	$p < 0.01$	-	$p < 0.02$

Abbreviations: CN, caudate nucleus; DGN, deep gray nuclei; GP, globulus pallidus; Put, putamen; RN, red nucleus; SN, substantia nigra; STN, subthalamic nucleus; -, statistically nonsignificant.

different magnetic susceptibility are strongly represented, but also by the more heterogeneous composition of brain tissues. Indeed, magnetic susceptibility in the human brain is mainly due to water, myelin, iron, and calcium.[3] If we still consider the background field-removal algorithms, the two most efficient pipelines for brain data (pipelines 4 and 6) used PDF and LBV,[33] respectively. Both algorithms showed similar performances in the literature in deep brain regions.[43] In our case, we also observed similar performances, but PDF allowed us to obtain better results (pipeline 4) concerning the statistical differences between the two age groups (Table 5). This is coherent with an already shown effect in former studies about the potential underperformances of LBV compared with PDF, due to more residual artifacts from the background field.[44] This could imply slightly higher magnetic susceptibility quantification variations between healthy volunteers. Moreover, PDF is among the background field-removal methods most recommended by the QSM Consensus Organization Committee.[19] The SHARP[34] algorithm and its variants (V-SHARP[31] and RESHARP[34]) were used in four of the 10 tested pipelines (pipelines 5 and 8 to 10). As is widely accepted, these algorithms are not necessarily accurate at brain boundaries. Former studies[19,43] pointed out that the underestimations may also be caused by inherent high pass filtering. This could be the reason why we observed recurrent lower magnetic susceptibility values in the SN (130 ± 19 voxels), which is one of the smallest volumes that we studied along with the RN (69 ± 10 voxels) and STN (26 ± 7 voxels). Using "nonexact" algorithms such as SHARP and its variants (V-SHARP and RESHARP) on such small volumes may result in a bias of lower or higher magnetic susceptibility values, compared with ranges from the literature, in the final quantification of susceptibility, as can be seen in Table 4. Our results confirmed the strong influence of the background field-removal algorithm used in the chosen pipelines, and can explain why the optimal pipelines for in vitro data are not the most adapted for in vivo data. The phase unwrapping algorithm also has an important role in the pipeline's efficiency. In pipeline 4, the ROMEO[30] algorithm was used. This is a path-based method, which is known to give an exact value for the unwrapped phase, whereas Laplacian algorithms (MEDI[27]), while robust, did not give the exact value of magnetic susceptibility. This pipeline 4 obtained the best quantitative and statistical results for brain data, certainly due to the combination of an exact phase unwrapping method and a boundary-robust algorithm at the background field-removal step. And yet, pipeline 4 was not able to obtain coherent results on phantoms, whatever the magnetic susceptibility range (Figure 3). Our study proved that the choice of algorithms, for the different steps of the QSM pipeline, strongly influences its performance in reconstructing precise QSM maps and providing an accurate magnetic susceptibility quantification. The best pipelines for in vitro studies are not the best for in vivo applications, and our results indicate the importance of always optimizing the QSM pipeline for objects or organs of interest and for the targeted magnetic susceptibility range. In this context, tools like SEPIA[18] are of major importance for comparing algorithms under the same conditions, given the multitude of scenarios (algorithms and their related parameters) that can be settled, for each step of QSM pipelines.

More generally, QSM challenges and ISMRM working group studies[19] are very useful, and particularly for proposing guidelines and reliable magnetic susceptibility values, which were crucial for evaluating our own results. For instance, although Guan et al.[16] (pipeline 5), Santin et al.[4] (pipeline 6), and Mao et al.[26] (pipeline 9) did not obtain strictly identical results concerning magnetic susceptibility quantification in human brain because of natural occurring variation and the aging effect, there is a consistency in the graduation of magnetic susceptibility values quantified in the DGN, whatever the age of the subjects, that we also observed in our study (Put < CN < RN < STN < SN < GP). Even although these three pipelines did not give the best results for our brain data, our magnetic susceptibility quantifications still gave results in the same ranges as these previous studies. Furthermore, concerning the STN, we managed to quantify magnetic susceptibility with several pipelines. But we still met a difficulty in validating our values, given the limited number of published results concerning this DGN. Despite the difficulty in identifying the most suitable pipelines, the obstacles associated with standardization, and the occasional lack of reliable data, this study confirms the effectiveness of the QSM method for quantifying magnetic susceptibility in DGN, in the context of aging: indeed, we obtained statistically significant differences between the YAG and the SAG for all DGN (Tables 4 and 5). Moreover, the *T2** data that we have also processed allowed us to affirm that the QSM pipelines tested were as efficient as *T2** for most of them and more efficient in the case of pipeline 4, as highlighted in previous studies.[12–14]

There are, however, some limitations to this study. First, as in other brain studies,[4,16,19,26] our work did not include any in vivo gold standard to validate our magnetic susceptibility quantifications in DGN. The gold standard would need to have a robust external reference. However, the masking and the background field-removal steps imply the suppression of any signal outside of the brain and therefore prevents the use of an external object with a known magnetic susceptibility range. In the absence of such a gold standard, we had to compare our results with other quantitative values reported in the literature. Another limitation concerns the masking step. Although recent recommendations[19] are to use or generate specific masks corresponding to each stage of the computation of the QSM map, in this study they were generated automatically by the FSL BET tool[38] for the echo combination, phase unwrapping, background field-removal, and dipole inversion steps. We carried out a random qualitative check on each stage, to ensure that no error was apparent. We did not find any irregularities such as holes in the dipole inversion reconstruction mask that could have led to incorrect magnetic susceptibility reconstruction. This step can, of course, be enhanced by using a more complete approach, such as the one detailed by the QSM Consensus Organization Committee et al.[19] We chose to use the mean magnetic susceptibility of the whole brain as the internal reference. However, because there is no consensus available, other studies may use different references, such as the white matter or cerebrospinal fluid (CSF). A recent study by Guan et al.[16] compared whole brain and CSF as reference and showed high correlation. In our case, the mean quantification on the whole brain (0 ± 0.001 ppm) and on the white matter (0 ± 0.003 ppm), averaged from all subjects and all pipelines, confirms that there is no systematic bias between the calculation approaches of the various pipelines. For phantoms, dilution is an additional challenge, as the smallest gadolinium concentrations require several aliquots to be built, leading to a potential

non-negligible deviation from the desired concentration values. In the case of studies dealing with homemade phantoms, it is then necessary to have an alternative reference method to accurately monitor the gadolinium concentration (i.e., using ICP-MS, as in our study). We are also aware that our in vivo database can be improved. First, as in many other referenced studies, our number of healthy volunteers was limited and increasing our database should be beneficial, particularly for statistical analysis, as shown in the recent study conducted by Guan et al. including 286 subjects.[16] However, we were able to obtain comparable SD with those found in the literature, even with a limited number of volunteers ($n = 20$). Second, our senior adults (age 46.8 ± 4.5 years) were generally younger than the senior groups of the references used to validate our results (Guan et al.[16]: 61.4 ± 7.8 years; Mao et al.[26]: 56.8 ± 10.7 years). This smaller age difference between the YAG and the SAG may be a cause of a less pronounced increase in magnetic susceptibility with age. However, our methodology still showed good accuracy and sensitivity, as it managed to efficiently differentiate these two groups. Our results of magnetic susceptibility quantification may also be biased by the DGN segmentation issue. We chose to overlay on QSM maps the segmentations of DGN obtained from T1w and T2w images (Figure 1). There are many studies using deep learning algorithms to directly segment DGN on the QSM maps,[16,45] which is another way to segment these brain structures. Also, atlases specific to PD are now becoming more efficient, such as HybraPD.[46] However, some structures are known to be difficult to segment, like the SN.[47] Our study did not highlight the best pipeline to use in the specific case of PD application and to target the magnetic susceptibility range of the DGN, but the most suitable of the 10 tested. Other pipelines are used in the literature,[10,15] particularly with the advent of deep learning methods like msQSM.[48]

A future step of our project will be to optimize our acquisition protocol to reduce the acquisition time as much as possible, without degrading the QSM data and the magnetic susceptibility quantification. The reduction of acquisition time could also enable improvement of the spatial resolution (ideally < 1 mm^3) and thus correct boundary bias in some reconstruction algorithms. This work will be followed by a clinical application on patients with PD, to explore the interest in magnetic susceptibility quantification as a new early neuromarker for PD.

5 | CONCLUSION

This study confirms that, to improve quantitative MRI methods, it is essential to go through two successive validation stages before considering an application on patients: first, in vitro on specific phantoms, then in vivo on healthy volunteers. Our results on specific phantoms showed the importance of optimizing QSM pipelines according to the clinical application and the targeted magnetic susceptibility range, to achieve an accurate quantification of magnetic susceptibility. Concerning in vivo results, our methodology allowed the quantification of magnetic susceptibility in all the brain regions of interest, and the definition of the optimal QSM pipeline for our future clinical application on PD, based on ROMEO, PDF, and MEDI algorithms.

Our results were consistent with those from the literature, despite a variability between these previous studies. We observed a tendency for magnetic susceptibility to increase with age, as expected, and statistically significant differences were obtained between the two age groups in Put ($p < 0.01$), CN ($p < 0.02$), STN ($p < 0.01$), SN ($p < 0.05$), RN ($p < 0.05$), and GP ($p < 0.02$). These preliminary results, achieved on small numbers of healthy volunteers ($n = 10$ per group), were convincing enough to validate our methodology and to consider its application on patients with PD.

The perspectives of this work are to explore the interest of magnetic susceptibility quantification as a new early neuromarker for PD. Our next goal is to make these new tools available to clinicians on standard clinical systems (i.e., 1.5 and 3 T) with limited acquisition times, so that they can be integrated into standard MRI protocols applied on patients with PD. These new neuromarkers will add to those already used in clinical routines, thus enabling early diagnosis of PD, improving the targeting of treatment offered to patients, and improving their quality of life.

ACKNOWLEDGMENTS

Part of this work has been performed using the PRISM core facility (Biogenouest, Univ Rennes, Univ Angers, INRAE, CNRS, France). In vivo MRI acquisition was performed at the Neurinfo MRI research facility (University of Rennes, Rennes University Hospital, INRIA, CNRS and Rennes Cancer Center). Neurinfo is also supported by Brittany Regional Council, Rennes Métropole and GIS IBISA. Finally, we would like to thank Matéo Jean, MS, for his contribution to the initial results of this study.

CONFLICT OF INTEREST STATEMENT

The authors declare no conflicts of interest.

DATA AVAILABILITY STATEMENT

The data that support the findings of this study are available on request from the corresponding author. The data are not publicly available due to privacy or ethical restrictions.

REFERENCES

1. Kalia LV, Lang AE. Parkinson's disease. *Lancet*. 2015;386(9996):896-912. doi:10.1016/S0140-6736(14)61393-3
2. Mahlknecht P, Seppi K, Poewe W. The concept of prodromal Parkinson's disease. *J Parkinsons Dis*. 2015;5(4):681-697. doi:10.3233/JPD-150685
3. Samson E, Noseworthy MD. A review of diagnostic imaging approaches to assessing Parkinson's disease. *Brain Disord*. 2022;6:100037. doi:10.1016/j.dscb.2022.100037
4. Santin MD, Didier M, Valabrègue R, et al. Reproducibility of R2* and quantitative susceptibility mapping (QSM) reconstruction methods in the basal ganglia of healthy subjects. *NMR Biomed*. 2017;30(4):e3491. doi:10.1002/nbm.3491
5. Tambasco N, Paolini Paoletti F, Chiappiniello A, et al. T2*-weighted MRI values correlate with motor and cognitive dysfunction in Parkinson's disease. *Neurobiol Aging*. 2019;80:91-98. doi:10.1016/j.neurobiolaging.2019.04.005
6. Dexter DT, Carayon A, Javoy-Agid F, et al. Alterations in the levels of iron, ferritin and other trace metals in Parkinson's disease and other neurodegenerative diseases affecting the basal ganglia. *Brain J Neurol*. 1991;114(Pt 4):1953-1975. doi:10.1093/brain/114.4.1953
7. Thomas GEC, Zarkali A, Ryten M, et al. Regional brain iron and gene expression provide insights into neurodegeneration in Parkinson's disease. *Brain J Neurol*. 2021;144(6):1787-1798. doi:10.1093/brain/awab084
8. Qu Z, Yang S, Xing F, et al. Magnetic resonance quantitative susceptibility mapping in the evaluation of hepatic fibrosis in chronic liver disease: a feasibility study. *Quant Imaging Med Surg*. 2021;11(4):1170-1183. doi:10.21037/qims-20-720
9. Zhao Z, Zhang L, Wen Q, et al. The effect of beta-amyloid and tau protein aggregations on magnetic susceptibility of anterior hippocampal laminae in Alzheimer's diseases. *Neuroimage*. 2021;244:118584. doi:10.1016/j.neuroimage.2021.118584
10. Li J, Nguyen TD, Zhang Q, Guo L, Wang Y. Cerebral microbleeds are associated with increased brain iron and cognitive impairment in patients with cerebral small vessel disease: a quantitative susceptibility mapping study. *J Magn Reson Imaging*. 2022;56(3):904-914. doi:10.1002/jmri.28092
11. Tan S, Hartono S, Welton T, et al. Utility of quantitative susceptibility mapping and diffusion kurtosis imaging in the diagnosis of early Parkinson's disease. *NeuroImage Clin*. 2021;32:102831. doi:10.1016/j.nicl.2021.102831
12. Barbosa JHO, Santos AC, Tumas V, et al. Quantifying brain iron deposition in patients with Parkinson's disease using quantitative susceptibility mapping, R2 and R2*. *Magn Reson Imaging*. 2015;33(5):559-565. doi:10.1016/j.mri.2015.02.021
13. Murakami Y, Kakeda S, Watanabe K, et al. Usefulness of quantitative susceptibility mapping for the diagnosis of Parkinson disease. *Am J Neuroradiol*. 2015;36(6):1102-1108. doi:10.3174/ajnr.A4260
14. Alkemade A, de Hollander G, Keuken MC, et al. Comparison of T2*-weighted and QSM contrasts in Parkinson's disease to visualize the STN with MRI. *PLoS ONE*. 2017;12(4):e0176130. doi:10.1371/journal.pone.0176130
15. Thomas GEC, Leyland LA, Schrag AE, Lees AJ, Acosta-Cabronero J, Weil RS. Brain iron deposition is linked with cognitive severity in Parkinson's disease. *J Neurol Neurosurg Psychiatry*. 2020;91(4):418-425. doi:10.1136/jnnp-2019-322042
16. Guan X, Guo T, Zhou C, et al. Altered brain iron depositions from aging to Parkinson's disease and Alzheimer's disease: a quantitative susceptibility mapping study. *Neuroimage*. 2022;264:119683. doi:10.1016/j.neuroimage.2022.119683
17. Hallgren B, Sourander P. The effect of age on the non-haemin iron in the human brain. *J Neurochem*. 1958;3(1):41-51. doi:10.1111/j.1471-4159.1958.tb12607.x
18. Chan KS, Marques JP. SEPIA-susceptibility mapping pipeline tool for phase images. *Neuroimage*. 2021;227:117611. doi:10.1016/j.neuroimage.2020.117611
19. QSM Consensus Organization Committee, Bilgic B, Costagli M, et al. Recommended implementation of quantitative susceptibility mapping for clinical research in the brain: a consensus of the ISMRM electro-magnetic tissue properties study group. *Magn Reson Med*. 2024;91(5):1834-1862. doi:10.1002/mrm.30006
20. Domínguez-Fernández C, Egiguren-Ortiz J, Razquin J, et al. Review of technological challenges in personalised medicine and early diagnosis of neurodegenerative disorders. *Int J Mol Sci*. 2023;24(4):3321. doi:10.3390/ijms24043321
21. Li KR, Avecillas-Chasin J, Nguyen TD, et al. Quantitative evaluation of brain iron accumulation in different stages of Parkinson's disease. *J Neuroimaging*. 2022;32(2):363-371. doi:10.1111/jon.12957
22. Olsson E, Wirestam R, Lind E. MRI-based quantification of magnetic susceptibility in gel phantoms: assessment of measurement and calculation accuracy. *Radiol Res Pract*. 2018;2018:6709525. doi:10.1155/2018/6709525
23. Deh K, Nguyen TD, Eskreis-Winkler S, et al. Reproducibility of quantitative susceptibility mapping in the brain at two field strengths from two vendors. *J Magn Reson Imaging*. 2015;42(6):1592-1600. doi:10.1002/jmri.24943
24. Fischl B. FreeSurfer. *NeuroImage*. 2012;62(2):774-781. doi:10.1016/j.neuroimage.2012.01.021
25. Manjón JV, Bertó A, Romero JE, et al. pBrain: a novel pipeline for Parkinson related brain structure segmentation. *NeuroImage Clin*. 2020;25:102184. doi:10.1016/j.nicl.2020.102184
26. Mao H, Dou W, Wang X, et al. Iron deposition in gray matter nuclei of patients with intracranial artery stenosis: a quantitative susceptibility mapping study. *Front Neurol*. 2022;12:785822. doi:10.3389/fneur.2021.785822
27. Liu T, Liu J, de Rochefort L, et al. Morphology enabled dipole inversion (MEDI) from a single-angle acquisition: comparison with COSMOS in human brain imaging. *Magn Reson Med*. 2011;66(3):777-783. doi:10.1002/mrm.22816
28. Liu J, Liu T, de Rochefort L, et al. Morphology enabled dipole inversion for quantitative susceptibility mapping using structural consistency between the magnitude image and the susceptibility map. *Neuroimage*. 2012;59(3):2560-2568. doi:10.1016/j.neuroimage.2011.08.082
29. Karsa A, Shmueli K. SEGUE: a Speedy rEgion-Growing Algorithm for Unwrapping Estimated phase. *IEEE Trans Med Imaging*. 2019;38(6):1347-1357. doi:10.1109/TMI.2018.2884093
30. Dymerska B, Eckstein K, Bachrata B, et al. Phase unwrapping with a rapid opensource minimum spanning tree algorithm (ROMEO). *Magn Reson Med*. 2021;85(4):2294-2308. doi:10.1002/mrm.28563
31. Li W, Wu B, Liu C. Quantitative susceptibility mapping of human brain reflects spatial variation in tissue composition. *Neuroimage*. 2011;55(4):1645-1656. doi:10.1016/j.neuroimage.2010.11.088
32. Liu T, Khalidov I, de Rochefort L, et al. A novel background field removal method for MRI using projection onto dipole fields (PDF). *NMR Biomed*. 2011;24(9):1129-1136. doi:10.1002/nbm.1670
33. Zhou D, Liu T, Spincemaille P, Wang Y. Background field removal by solving the Laplacian boundary value problem. *NMR Biomed*. 2014;27(3):312-319. doi:10.1002/nbm.3064

34. Sun H, Wilman AH. Background field removal using spherical mean value filtering and Tikhonov regularization. *Magn Reson Med*. 2014;71(3):1151-1157. doi:10.1002/mrm.24765
35. Wei H, Dibb R, Zhou Y, et al. Streaking artifact reduction for quantitative susceptibility mapping of sources with large dynamic range. *NMR Biomed*. 2015;28(10):1294-1303. doi:10.1002/nbm.3383
36. Wharton S, Schäfer A, Bowtell R. Susceptibility mapping in the human brain using threshold-based *k*-space division. *Magn Reson Med*. 2010;63(5):1292-1304. doi:10.1002/mrm.22334
37. Wang C, Martins-Bach AB, Alfaro-Almagro F, et al. Phenotypic and genetic associations of quantitative magnetic susceptibility in UK Biobank brain imaging. *Nat Neurosci*. 2022;25(6):818-831. doi:10.1038/s41593-022-01074-w
38. Smith SM. Fast robust automated brain extraction. *Hum Brain Mapp*. 2002;17(3):143-155. doi:10.1002/hbm.10062
39. Guan X, Xuan M, Gu Q, et al. Influence of regional iron on the motor impairments of Parkinson's disease: a quantitative susceptibility mapping study. *J Magn Reson Imaging*. 2017;45(5):1335-1342. doi:10.1002/jmri.25434
40. Gustavo Cuña E, Schulz H, Tuzzi E, et al. Simulated and experimental phantom data for multi-center quality assurance of quantitative susceptibility maps at 3 T, 7 T and 9.4 T. *Phys Med*. 2023;110:102590. doi:10.1016/j.ejmp.2023.102590
41. Hobson N, Polster SP, Cao Y, et al. Phantom validation of quantitative susceptibility and dynamic contrast-enhanced permeability MR sequences across instruments and sites. *J Magn Reson Imaging*. 2020;51(4):1192-1199. doi:10.1002/jmri.26927
42. Silva J, Milovic C, Lambert M, et al. Toward a realistic in silico abdominal phantom for QSM. *Magn Reson Med*. 2023;89(6):2402-2418. doi:10.1002/mrm.29597
43. Schweser F, Robinson SD, de Rochefort L, Li W, Bredies K. An illustrated comparison of processing methods for phase MRI and QSM: removal of background field contributions from sources outside the region of interest. *NMR Biomed*. 2017;30(4):e3604. doi:10.1002/nbm.3604
44. Zhu X, Gao Y, Liu F, Crozier S, Sun H. BFRnet: a deep learning-based MR background field removal method for QSM of the brain containing significant pathological susceptibility sources. *Z Für Med Phys*. 2023;33(4):578-590. doi:10.1016/j.zemedi.2022.08.001
45. Yoon J, Gong E, Chatnuntawech I, et al. Quantitative susceptibility mapping using deep neural network: QSMnet. *Neuroimage*. 2018;179:199-206. doi:10.1016/j.neuroimage.2018.06.030
46. Yu B, Li L, Guan X, et al. HybraPD atlas: towards precise subcortical nuclei segmentation using multimodality medical images in patients with Parkinson disease. *Hum Brain Mapp*. 2021;42(13):4399-4421. doi:10.1002/hbm.25556
47. Tessema AW, Lee H, Gong Y, et al. Automated volumetric determination of high R_2^* regions in substantia nigra: a feasibility study of quantifying substantia nigra atrophy in progressive supranuclear palsy. *NMR Biomed*. 2022;35(11):e4795. doi:10.1002/nbm.4795
48. He J, Peng Y, Fu B, Zhu Y, Wang L, Wang R. msQSM: morphology-based self-supervised deep learning for quantitative susceptibility mapping. *Neuroimage*. 2023;275:120181. doi:10.1016/j.neuroimage.2023.120181

How to cite this article: Hervouin A, Bézy-Wendling J, Noury F. How to accurately quantify brain magnetic susceptibility in the context of Parkinson's disease: Validation on phantoms and healthy volunteers at 1.5 and 3 T. *NMR in Biomedicine*. 2024;e5182. doi:10.1002/nbm.5182